The connection between halo concentrations and assembly histories: a probe of gravity?

Piotr Oleśkiewicz[1]*, Carlton M. Baugh[1], Aaron Ludlow[2],
[1] *Institute for Computational Cosmology, Department of Physics, Durham University, South Road, Durham DH1 3LE, UK*
[2] *International Centre for Radio Astronomy Research, University of Western Australia, 35 Stirling Highway, Crawley, Western Australia 6009, Australia*

Accepted XXX. Received YYY. in original form ZZZ

ABSTRACT
We use two high resolution N-body simulations, one assuming general relativity and the other the Hu-Sawicki form of $f(R)$ gravity with $|\bar{f}_R| = 10^{-6}$, to investigate the concentration–formation time relation of dark matter haloes. We assign haloes to logarithmically spaced mass bins, and fit median density profiles and extract median formation times in each bin. At fixed mass, haloes in modified gravity are more concentrated than those in GR, especially at low masses and at low redshift, and do not follow the concentration–formation time relation seen in GR. We assess the sensitivity of the relation to how concentration and formation time are defined, as well as to the segregation of the halo population by the amount of gravitational screening. We find a clear difference between halo concentrations and assembly histories displayed in modified gravity and those in GR. Existing models for the mass–concentration–redshift relation that have gained success in cold and warm dark matter models require revision in $f(R)$ gravity.

Key words: dark matter – galaxies: haloes – methods: numerical

1 INTRODUCTION

N-body simulations have driven astounding progress in improving our understanding of gravitational collapse and its role in the formation of cosmic structure and galaxy evolution. For example, simulations have demonstrated that the mass distribution inside dark matter haloes follows an approximately universal form that can be specified by only two parameters (Navarro et al. 1996, 1997, hereafter NFW collectively):

$$\frac{\rho(r)}{\rho_{\rm crit}} = \frac{\delta_{\rm c}}{(r/r_{-2})\,(1+r/r_{-2})^2}, \tag{1}$$

where r_{-2} is a scale radius (at which the logarithmic slope of the density profile is equal to -2), and $\delta_{\rm c}$ is a characteristic overdensity. It is common to recast these into other forms, such as halo virial[1] mass, M_{200}, and concentration, $c = r_{200}/r_{-2}$ (the ratio of the virial and scale radii). At fixed M_{200}, $\delta_{\rm c}$ is given by

$$\delta_c = \frac{200}{3}\frac{c^3}{\ln(1+c) - c/(1+c)}, \tag{2}$$

such that higher concentration implies higher characteristic density.

Simulations of structure growth in the cold dark matter model (CDM) have also revealed a well-defined, redshift-dependent correlation between these parameters: at fixed redshift concentrations decrease with increasing mass, and at fixed mass decrease with increasing redshift (see, e.g., Bullock et al. 2001; Gao et al. 2008). These trends betray an simpler relation between the characteristic density of a halo and its formation time, $z_{\rm f}$: haloes that form early have, on average, higher $\delta_{\rm c}$ than late-forming ones, reflecting the higher background density at that time (e.g., Neto et al. 2007; Ludlow et al. 2013). This fact has been used to construct a number of empirical models for the concentration-mass-redshift relation (hereafter $c(M,z)$, for short) that appeal to various definitions of formation time to predict characteristic densities, and hence concentrations (e.g., NFW; Bullock et al. 2001; Wechsler et al. 2002; Zhao et al. 2003; Macciò et al. 2008; Zhao et al. 2009; Ludlow et al. 2014a; Correa et al. 2015; Ludlow et al. 2016).

Various models have met with varied success, plausibly due to diverse definitions of collapse time (see, e.g., Neto et al. 2007; Ludlow et al. 2016, for details). Several studies define the formation time of a halo as the point at which some fraction F of its final virial mass had first assembled, either into one *main* progenitor or accumulated over many small progenitors. However, as first discussed in Ludlow et al. (2013), better agreement with simulation re-

---

* E-mail: piotr.oleskiewicz@durham.ac.uk

[1] We define the virial mass, $M_{200} = (800/3)\,\pi\, r_{200}^3\, \rho_{\rm crit}$, and corresponding virial radius, r_{200}, as that of a sphere (centred on the particle with the minimum potential energy) whose mean density is equal to 200 times the critical density, $200 \times \rho_{\rm crit}$.

sults can be obtained by defining $z_{\rm f}$ in terms of the halo's *characteristic* mass, $M_{-2} = M(< r_{-2})$, rather than M_{200} (we elaborate on this point in Section 2.2). This has inspired a number of empirical models that successfully reproduce the $c(M, z)$ relation in both cold (Ludlow et al. 2014a; Correa et al. 2015) and warm dark matter cosmologies (Ludlow et al. 2016)

As a result, there exists an increasingly well-described relation between halo mass and concentration (Duffy et al. 2008; Prada et al. 2012; Angel et al. 2016; Klypin et al. 2016; Diemer & Kravtsov 2015; Diemer & Joyce 2019)–the two parameters that are needed to specify the density profile of a relaxed dark matter halo–and how they evolve with time. Further, both analytic and empirical models have been shown to describe reasonably well the $c(M, z)$ relation for a variety of cosmological parameters and power spectra. Our objective here is to investigate whether the relation between concentration and formation time–upon which many of these models are based–is sensitive to the gravitational force law, as stark differences could be used to probe departures from general relativity.

Proposals for modifications to general relativity (GR) were originally motivated by trying to solve one of the biggest remaining problems with the concordance ΛCDM: the origin of the accelerated cosmic expansion. ΛCDM achieves this by invoking a cosmological constant, Λ, but the required value is difficult to justify from a theoretical viewpoint (Carroll et al. 2004). Many alternatives have been proposed to the standard ΛCDM model: the accelerated expansion could be driven by as-of-yet unknown physics in the dark sector (Zuntz et al. 2010) or by a modification to GR itself (Koyama 2016). Among the alternatives to GR, one of the most widely studied is $f(R)$ gravity – an umbrella term referring to modified gravity models which change the Ricci scalar in Einstein-Hilbert action (Buchdahl 1970; Clifton et al. 2012; Joyce et al. 2015). Current versions of the theory are fine-tuned to match the expansion history in ΛCDM, which removes some of the model's original appeal. Nevertheless, $f(R)$ gravity remains a workable alternative to GR with interesting phenomenology. While the parameter space of $f(R)$ models is already tightly constrained by observations (Lombriser 2014), there still exists a range of models which may display measurable differences from GR (see, for example, He et al. 2018; Hernández-Aguayo et al. 2018).

Our study uses the merger histories of dark matter haloes traced back to progenitors that are two orders of magnitude less massive than the final halo mass. Hence, high resolution simulations are necessary (see Table 1). We therefore use the LIMINALITY simulations of Shi et al. (2015), a suite of very high resolution dark-matter-only runs including examples of the Hu & Sawicki (2007, HS) parametrisation of $f(R)$ gravity. Two simulations are compared: one of GR and another $f(R)$ modified gravity model that is compatible with current observational constraints.

This paper is structured as follows. The theoretical background is given in Section 2: the $f(R)$ model is discussed in Section 2.1, a description of the $c(M, z)$ model of Ludlow et al. (2016) in Section 2.2; the methods for building halo catalogues and merger trees are described in Section 2.3 and Section 2.4, respectively. Our results are presented in Section 3. Halo selection is outlined in Section 3.1, and the processing (fitting density profiles and estimating formation times) is covered in Sections 3.2 and 3.3. The concentration – formation time relation obtained from the processed simulation data is presented in Section 3.4. We explore the sensitivity of the model predictions to the parameter choices that specify the model in Section 3.5, and to the segregation of the halo population by the effectiveness of the screening of the gravity fifth force in Section 3.6. Finally, in Section 4, we present our conclusions. Results obtained by fitting Einasto (1965) (rather than NFW) profiles to determine halo structural parameters are discussed in Appendix A.

2 THEORY

2.1 $f(R)$ gravity

As mentioned in the Introduction, the motivation behind the original $f(R)$ model was to provide an elegant theoretical explanation for the observed accelerated expansion of the Universe (Buchdahl 1970). However, in practice $f(R)$ models are, by construction, fine-tuned to match the expansion history of the ΛCDM Universe, which has been tightly constrained (Hinshaw et al. 2013; Planck Collaboration et al. 2016). In $f(R)$ gravity, the Einstein-Hilbert action is modified by adding an extra term to the Ricci scalar R

$$S = \frac{1}{16\pi G}\int {\rm d}^4x\sqrt{-g}\left[R + f(R)\right]. \qquad (3)$$

The $f(R)$ term causes an increase in the strength of the gravitational force compared to GR. In order to satisfy astrophysical constraints on gravity (Lombriser 2014; Cataneo et al. 2015; Nunes et al. 2017), the theory contains a chameleon screening mechanism (Khoury & Weltman 2004) which means that the GR-strength force is recovered in dense environments.

From Eq (3) we can derive the Poisson equation for modified gravity

$$\frac{1}{a^2}\vec{\nabla}^2\phi = \frac{16\pi G}{3}\left(\rho_m - \bar{\rho}_m\right) + \frac{1}{6}\left(R\left(f_R\right) - \bar{R}\right), \qquad (4)$$

where $f_R = {\rm d}f/{\rm d}R$ and bars on top of variables signify background values. The equation remains valid for $|f(R)| \ll |\bar{R}|$ and $|f_R| \ll 1$, both of which hold for the model we are investigating. Evidently, the only difference with respect to the Newton-Poisson equation depends solely on f_R, the derivative of f with respect to R. The magnitude of f_R relative to the classical Newtonian potential, ϕ, splits the equation into two regimes:

(i) $|f_R| \ll |\phi|$: gravity is to a good approximation described by GR, with no increased strength; these regions are called "screened".

(ii) $|f_R| \geq |\phi|$: the Poisson equation is enhanced by a factor of 1/3; in these regions screening is ineffective.

Hence, in $f(R)$ models the strength of gravity is always between 1 and 4/3 times the GR value. While the particular choice of $f(R)$ determines the shape of the gravitational potential in the unscreened regions, it does not affect the strength of the fifth force or the effectiveness of the screening mechanism, which is only determined by the magnitude of its derivative $|f_R|$. For this reason the models are characterised by $|\bar{f}_R|$ with, e.g., F6 denoting $|\bar{f}_R| = 10^{-6}$.

Table 1. Relevant parameters of the LIMINALITY N-body simulations from Shi et al. (2015).

Ω_m	(matter density)	0.281
Ω_Λ	(dark energy density)	0.719
Ω_b	(baryon density)	0.046
σ_8	(power spectrum amplitude)	0.820
n_s	(spectral index)	0.971
h	$(H_0/[100\,\mathrm{km\,s^{-1}\,Mpc^{-1}}])$	0.697
L	(box side)	$64h^{-1}$Mpc
M_p	(particle mass)	$1.523\times10^8h^{-1}\mathrm{M}_\odot$
N_p	(particle number)	512^3
z_final	(final redshift)	0.0
z_0	(initial redshift)	49.0
N_out	(number of outputs)	122

Astrophysical constraints limit the choices of the present day background value of $|\bar{f}_R|$. Supernovae (Upadhye & Steffen 2013), X-ray (Terukina et al. 2014) and Solar System (Berry & Gair 2011; Lombriser et al. 2014) observations already rule out models with $|\bar{f}_R| > 10^{-5}$ (F5, F4, etc.). On the contrary, cosmologies with $|\bar{f}_R| \leq 10^{-7}$ show negligible differences to GR in terms of structure formation. Here we investigate the similarities and differences between the GR and F6 ($|\bar{f}_R| = 10^{-6}$) simulations.

The best-studied $f(R)$ model, Hu & Sawicki (2007, HS) gravity, introduces an empirical definition of f:

$$f(R) = -M^2\frac{c_1\left(-R/M^2\right)^n}{c_2\left(-R/M^2\right)^n+1}, \tag{5}$$

where c_1 and c_2 control the screening threshold, $|f_{R0}| = c_1/c_2^2$, and $M = H_0^2/\Omega_\mathrm{m}$ is determined by the cosmology through its dependence on the Hubble constant, H_0, and matter density parameter, Ω_m.

As the equations describing the modifications to standard gravity are non-linear, modified gravity simulations are more demanding of computational resources than their standard gravity counterparts of the same size and resolution. However, significant progress has been made recently in numerical techniques designed specifically for this class of theories (Li et al. 2012; Bose et al. 2015). We focus our analysis on the LIMINALITY simulation (Shi et al. 2015), a high-resolution, N-body simulation of HS F6 modified gravity. For comparison, a GR simulation with otherwise identical cosmology is also studied. The cosmological parameters of both runs (Table 1) have been tuned to match the `WMAP9` cosmology (Hinshaw et al. 2013).

2.2 Mass-Concentration-Redshift relation

The $c(M, z)$ model tested here, first described in Ludlow et al. (2016), uses the extended Press-Schechter (EPS) formalism to approximate the gravitational collapse of collisionless DM haloes (Bond et al. 1991; Mo et al. 2010). In EPS, the *collapsed mass history* (hereafter CMH), $M(z)$, of a dark matter halo (i.e. the sum of progenitor masses at redshift z exceeding $f \times M_{200}(z_0)$) identified at redshift z_0 is given by

$$\frac{M(z)}{M_0} = \mathrm{erfc}\left(\frac{\delta_\mathrm{sc}(z)-\delta_\mathrm{sc}(z_0)}{\sqrt{2(\sigma^2(f\times M_0)-\sigma^2(M_0))}}\right). \tag{6}$$

Here $M_0 = M_{200}(z_0)$ is mass at the identification redshift, $\sigma^2(m)$ is the variance of the density field smoothed with a spherical top-hat window function containing mass m, and $\delta_\mathrm{sc}(z) \approx 1.686/D(z)$ is the redshift-dependent spherical collapse threshold, with $D(z)$ the linear growth factor.

One difference between the EPS theory and the Ludlow et al. (2016) scheme is the definition of halo formation time: in EPS, a common definition of a formation redshift, z_f, is the one at which the sum of progenitor masses more massive than $f \times M_{200}$ first exceeds a fraction $F \times M_{200}$, where typically $f = 0.01$, $F = 0.5$ (e.g. Lacey & Cole 1993; Navarro et al. 1996). In Ludlow et al. (2016), F is not a parameter, but varies between the haloes and can be calculated from their concentration:

$$F = \frac{M_{-2}}{M_{200}} = \frac{\ln(2)-1/2}{\ln(1+c)-c/(1+c)}, \tag{7}$$

where the right-most equation is strictly valid for an NFW profile. For each halo, z_f therefore corresponds to the redshift at which a fraction M_{-2}/M_{200} of the halo's final mass had first assembled into progenitors more massive than $f \times M_{200}$ (where $f = 0.02$). Ludlow et al. (2016) referred to this redshift as z_{-2}, to annotate its explicit dependence on the characteristic mass, M_{-2}.

The CMH is scale invariant in both CDM and warm dark matter (WDM) models, and can be used to estimate z_{-2} and the corresponding critical density, $\rho_\mathrm{crit}(z_{-2})$. The $c(M, z)$ model advocated by Ludlow et al. (2016) exploits the strong, linear correlation between $\rho_\mathrm{crit}(z_{-2})$ and $\langle\rho_{-2}\rangle$, the mean density within r_{-2}. Empirically, they found $\langle\rho_{-2}\rangle = A \times \rho_\mathrm{crit}(z_{-2})$, with $A \approx 400$. Once the CMH is known, this expression can be used to compute $\langle\rho_{-2}\rangle$, and hence infer the halo mass profile.

The model accurately reproduces the concentrations of dark matter haloes in both CDM and WDM cosmologies. This may appear surprising at first as dark matter haloes in WDM simulations have been found to display different concentrations and formation times than in CDM (Macciò et al. 2013; Bose et al. 2016). However, these changes act to preserve the $\langle\rho_{-2}\rangle - \rho_\mathrm{crit}(z_{-2})$ relation seen in CDM.

It has been shown that haloes in $f(R)$ cosmologies follow NFW density profiles (Lombriser 2014) like their GR counterparts, but with systematically higher concentrations. Their assembly histories also differ, but only slightly (Shi et al. 2015). Hence, it might be expected that the relation discovered by Ludlow et al. (2016) for CDM and WDM haloes in standard gravity might hold for $f(R)$ haloes only under certain conditions: (i) for small values of $|f_{R0}|$, and (ii) for all haloes *except* low-mass objects at low redshifts, due to screening. It is therefore plausible that the above concentration – formation time relation will not be applicable to the full population of haloes in $f(R)$ gravity, and this is the hypothesis that we test here. This breakdown could potentially be circumvented by either re-parametrising the model or segregating haloes to reflect the influence of the fifth force, which we explore later.

2.3 Halo identification

The gravitational collapse of collisionless CDM can be approximated by the spherical collapse model (Gunn & Gott 1972; Peebles 1980; but see Ludlow et al. 2014b). In this model, overdensities collapse to form dark matter haloes, which are defined as isolated regions with an average matter density larger than a threshold $\Delta_{\rm vir} \approx 178\,(\approx 200)$ times the critical density (Mo et al. 2010, Ch. 5).

Because we are primarily concerned with the GR / $f\,(R)$ comparison, we have elected to use r_{200} to define halo virial radii and M_{200} for the corresponding masses. This convention follows that of Ludlow et al. (2016) and is based on the fact that, while r_{200} remains well-defined and is independent of the gravity model, the virial parameters vary systematically with the strength of gravity (Schmidt et al. 2009). The virial mass and radius therefore define a sphere (centred on the particle with the minimum potential energy) that encloses a mean density equal to 200 times the critical density, $\rho_{\rm crit}\,(z)$, and are thus labelled with the subscript 200.

Subhaloes are locally overdense regions within haloes, and are the surviving remnants of past mergers. Haloes are initially identified using a friends-of-friends (FoF) algorithm (Davis et al. 1985). The halo catalogue is then processed using an upgraded version of `HBT` (Han et al. 2012, Hierarchical Bound-Tracing algorithm), `HBT+` (Han et al. 2018), which identifies subhaloes and builds their merger trees.

`HBT+` is a publicly available[2] merger tree code, which identifies subhaloes and follows them between simulation outputs, from the earliest snapshot at which they can be identified until the final one, building a merger tree from the catalogue on-the-fly. A list of gravitationally bound particles is created for each halo; these are used to identify a descendant (a halo at a lower redshift, sharing subhaloes), and are passed to the successive snapshot. Each halo can have one or more progenitors (haloes at a higher redshift, sharing subhaloes). If a halo has multiple progenitors, the most massive one is selected, and it becomes the ”main” (i.e. most massive) subhalo. Other progenitors are mapped to the subhaloes which belong to the host halo. The host halo of a subhalo is the FoF halo containing its most bound particle.

2.4 Merger trees

The merger tree of a halo, visualised in Fig. 1, can be obtained from the `HBT+` output by following the progenitors of a given halo, recording their host haloes, and repeating this process recursively until the earliest progenitors are reached in each branch. However, the trees produced by this procedure have two common defects[3]:

(i) Re-mergers, such as the right-most halo in the second row in Fig. 1, happen when one of the subhaloes temporarily becomes gravitationally unbound and is identified as a separate halo for one or more snapshots; in a later snapshot it merges back into the original host halo, creating a “loop”. The halo in the “loop” is retained as a progenitor halo and so re-mergers do not alter the collapsed mass history (which sums over the masses of progenitors at any given snapshot, and as such is not affected by the order or the sequence of the mergers). This is similar to the scheme used to build merger trees by Jiang et al. (2013).

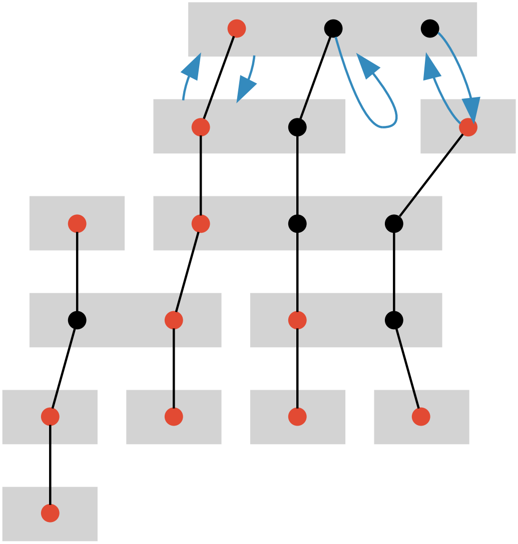

Figure 1. A schematic representation of a merger tree with two defects: a re-merger (halo in the second row down, on the right) and a fly-by (halo in the third row down on the left). Grey rectangles represent haloes, and dots subhaloes; every halo has one main subhalo, marked with a red dot; subhaloes are matched between snapshots (black lines) by following the most bound particles. The blue arrows indicate the relationships relevant in building merger trees, and represent (left to right): (i) halo descendant, (ii) halo progenitor, (iii) host of a subhalo, (iv) host of subhaloes’ progenitor, (v) descendant of a subhalo. This plot can be compared with similar diagrams included in Thomas et al. (2015); Han et al. (2018).

(ii) Fly-bys (e.g. the branch merging into, and then leaving, the left-most halo in the fourth row down in Fig. 1) happen when a subhalo is identified as a part of a FoF halo for one or more snapshots due to a temporary spatial overlap, but later becomes an isolated halo again. The presence of fly-bys pollutes the CMH, artificially inflating the mass at snapshots with extra subhaloes.

Both defects can be avoided by only keeping those haloes in the tree which merge as the main subhaloes of the host in the preceding snapshot (which would remove both example defects shown in Fig. 1). This is not equivalent to keeping only the main branch of the halo mass history – the full CMH is still used, but it is calculated from a pruned merger tree.

3 RESULTS

Our goal is to determine the relation between halo concentration (or more specifically $\langle\rho_{-2}\rangle$) and the critical density at the formation time z_{-2} (namely $\rho_{\rm crit}(z_{-2})$) for haloes of different masses at different redshifts. For each mass bin we construct the median density profile and CMH, which are used to estimate median concentration and formation time. This approach has the benefit of producing smoother profiles, and in turn a smoother density-density relation, as is

---

[2] https://github.com/Kambrian/HBTplus

[3] Technically, these are not trees as they contain loops, and some nodes might have more than one parent node.

evident from comparing Fig. 3 from Ludlow et al. (2013) and Fig. 7 from Ludlow et al. (2016).

This section outlines the details of each step of our analysis. The source code used for the analysis is publicly available[4].

3.1 Filtering & binning

Our halo catalogues are obtained by filtering the `HBT+` output and retaining objects with a minimum of 20 particles. Since we are interested in resolving the merger history of haloes down to progenitors with $f = 0.02$ times their final mass, this places a lower limit of $n_{200} = 10^3$ on the number of particles a halo must contain in order to be included in our analysis.

Haloes are divided into bins that are equally-spaced in $\log_{10}(M_{200}/[h^{-1}M_\odot])$, with $\Delta\log_{10}(M_{200}/[h^{-1}M_\odot]) = 0.162$. To identify potentially unrelaxed systems we use the centre-of-mass offset parameter,

$$d_{\rm off} = \frac{|\mathbf{r}_p - \mathbf{r}_{\rm CM}|}{r_{200}}, \tag{8}$$

where $\mathbf{r}_p$ is the centre of potential, and $\mathbf{r}_{\rm CM}$ the centre-of-mass (Thomas et al. 2001; Maccio et al. 2007; Neto et al. 2007). Only haloes with $d_{\rm off} < 0.07$ are retained for analysis.

The fitting of mass profiles (Section 3.2) and calculation of formation times (Section 3.3) is performed on the median mass profiles and CMHs, respectively, for each mass bin.

3.2 Fitting mass profiles

The cumulative mass profile is defined using all particles within r_{200}, and not only those deemed *bound* to the main halo or its subhaloes. These particles are assigned to logarithmically spaced radial bins, within which enclosed masses are computed. The mass profiles of haloes in each mass bin are assigned in this way, and their median is calculated. Finally, the median mass profile is normalised by the total median enclosed mass, $M_{200} = M(r < r_{200})$. The best-fitting value of the concentration, c, is obtained by minimising

$$\chi^2 = \sum_{i=0}^{20} \left[\log_{10}(M_i) - \log_{10}(M(r < r_i, c))\right]^2, \tag{9}$$

where M_i is the mass measured within r_i, $M(<r, c)$ is the mass enclosed within radius r for an NFW profile with a concentration c (Eq (1)); quantities with subscript i refer to the $i^{\rm th}$ bin in $\log_{10}$ radius from the halo centre.

We have used both NFW and Einasto profiles in our analysis. Results for NFW profiles are provided in the main text and Einasto profiles are discussed in Appendix A, for completeness. Appendix A shows that the quality of fit does not improve sufficiently to warrant using the Einasto profile (which has an extra parameter) over NFW. We emphasise that the choice of analytic density profile does not change our results or conclusions.

Our fits to Eq (9) are minimised over the radial range $r_{\rm min} < r_i < r_{\rm max}$, where $r_{\rm min}$ is a minimum fit radius, and $r_{\rm max}$ is set to $0.8 \times r_{200}$ to exclude the unrelaxed outer edges of haloes (Ludlow et al. 2010). We consider two definitions of $r_{\rm min}$:

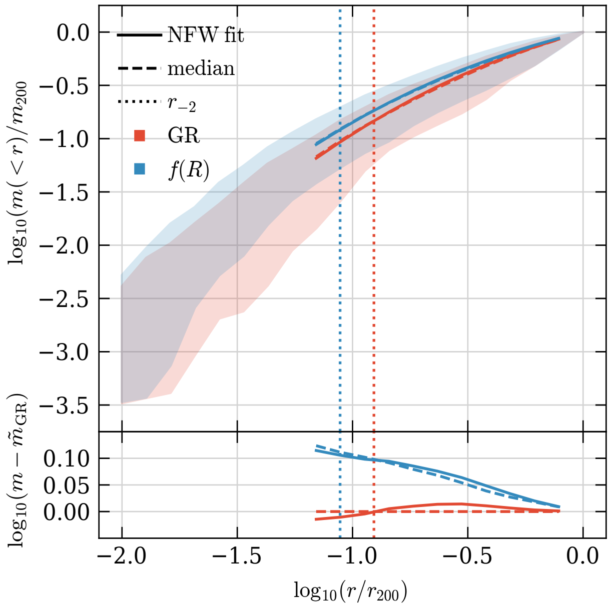

Figure 2. Radial enclosed mass profiles for haloes in the mass range $11.5 < \log_{10}(M_{200}/[h^{-1}M_\odot]) < 11.7$ at $z_0 = 0$. GR and $f(R)$ runs are shown using red and blue curves, respectively, as indicated in the legend; residuals from GR are shown in the lower panel. The faint shading shows the envelope of the individual mass profiles; dashed lines show median mass profiles; solid lines show the best fitting NFW profiles to the median mass profiles, for radii between $r_{\rm min} < r < r_{\rm max}$; vertical dotted lines show the characteristic scale r_{-2}. Residuals are taken from the median mass profile of GR haloes, $\tilde{m}_{\rm GR}$.

(i) half of the mean particle separation within r_{200} (Moore et al. 1998),

$$r_{\rm min} = \frac{1}{2}\left(\frac{4\pi}{3n_{200}}\right)^{1/3} r_{200}, \tag{10}$$

where n_{200} is the number of particles enclosed within r_{200}, and

(ii) the radius at which the two-body relaxation time is equal to the age of the universe, t_0 (Power et al. 2003; Ludlow et al. 2018), which can be approximated by the solution to

$$\frac{t_{\rm relax}(r)}{t_0} = \frac{\sqrt{200}}{8}\frac{n(<r)}{\ln(n(<r))}\left(\frac{\langle\rho(<r)\rangle}{\rho_{\rm crit}}\right)^{-1/2}. \tag{11}$$

Here $n(<r)$ is the number of particles enclosed by radius r and $\langle\rho(<r)\rangle$ is the mean enclosed density, $\langle\rho(<r)\rangle = 3m(<r)/4\pi r^3$.

Although we have considered both options, results are shown for the Moore et al. (1998) definition as it is typically more conservative than the alternative. Henceforth, all $r_{\rm min}$ values are calculated using Eq (10).

Once c is found, M_{-2} can be calculated from Eq (7); the characteristic density of the halo is then given by $\langle\rho_{-2}\rangle = 3\,M_{-2}/4\,\pi\,r_{-2}^3$.

---

[4] `https://doi.org/10.5281/zenodo.2593623`

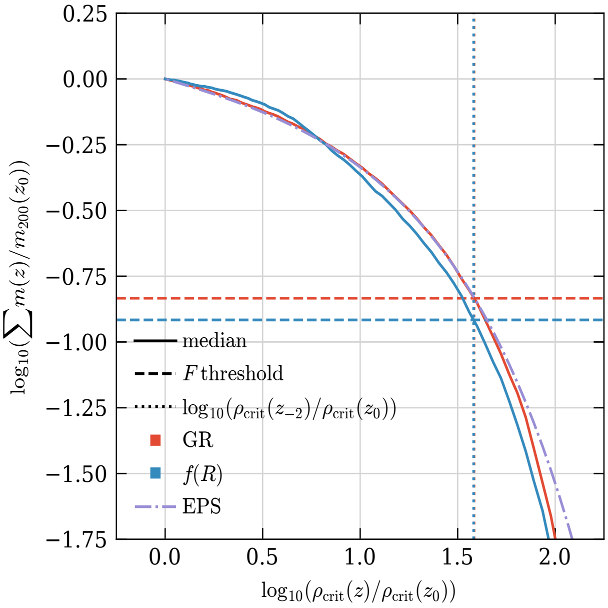

Figure 3. Median collapsed mass histories (CMHs) for haloes in the mass range $11.5 < \log_{10}\left(M_{200}/[h^{-1}M_\odot]\right) < 11.7$ at $z_0 = 0$. As with Fig. 2, GR and $f(R)$ runs are shown using red and blue lines, respectively. Solid lines show the median collapsed mass histories; two dotted vertical lines indicate the formation times, z_{-2}, at which the CMHs drop below a fraction $F = M_{-2}/M_{200}$ of the virial mass at z_0, plotted as two horizontal dashed lines. Note that despite the difference in F, derived from concentrations shown in Fig. 2, z_{-2} values are indistinguishable. The purple dashed-dot line shows the EPS prediction from Eq (6) for M_0 equal to median mass in this bin.

3.3 Calculating halo formation times

The mass growth history of a dark matter halo, $m(z)$, can be defined in different ways. The mass assembly history (MAH) is the mass history of a halo obtained using a "greedy" algorithm, by following the most massive (or main) progenitor through all snapshots and storing its M_{200}. As discussed previously, the collapsed mass history (CMH) is defined as the sum of the masses $M_{200,i}$ of every progenitor i whose virial mass exceeds $f \times M_0$, where f is a model parameter (we use 0.02 as our default value, but consider alternatives as well), and M_0 is M_{200} of the root halo. The CMH therefore takes into account all branches of the merger tree at a given snapshot.

The CMH can be obtained by gathering all progenitors of a halo from the merger tree, and summing over the masses of the progenitors at each snapshot. However, for performance reasons, the step of building a tree can be skipped in favour of searching for all progenitors of a root halo at each preceding snapshot. In other words, since the halo masses are summed over, it is not the structure of the merger tree that matters but its members.

Once the median CMH is calculated for each mass bin, it is normalised by the final mass M_0 at redshift z_0. For each mass bin, a formation time z_{-2} can then be calculated. This is defined as the time at which the CMH first exceeds a fraction $F = M_{-2}/M_0$ (calculated for a given mass bin from Eq (7)) of the final mass, M_0:

$$z_{-2} = z \ni \frac{M(z)}{M(z_0)} = F. \qquad (12)$$

The formation time may be ill-defined for non-monotonic assembly histories. The monotonic behaviour of the CMH, while difficult to guarantee for individual haloes, is in practice obtained by considering the median CMH of all haloes in each mass bin (as opposed to calculating formation times of individual haloes, binning the haloes and then taking the median in each mass bin). As simulations have a finite number of outputs, and hence finite time resolution, the value of the formation time is obtained using linear interpolation between the snapshots which are immediately before and after the crossing of the formation threshold fraction.

Examples of the median CMHs for $z = 0$ haloes in a narrow bin of M_{200} are shown in Fig. 3. Solid red curves correspond to our GR simulation, and blue to $f(R)$. An analytic prediction from Eq (6), as discussed in Ludlow et al. (2016), is plotted in a purple dashed-dot line; the result agrees quite well with the CMHs obtained from *both* simulations. For example, the formation times, z_{-2} (vertical dotted lines of corresponding color), agree with one another to $\approx 5\%$. Nevertheless, despite similarities in CMHs, these haloes *do not* have similar concentrations. The horizontal dashed lines correspond to M_{-2}/M_{200}, which show clear differences; indeed, concentration is 30% larger in $f(R)$ than in GR.

3.4 The density–density relation

The above analysis was carried out at $z_0 = 0$, 0.5, 1, 2 and 3. At each snapshot, haloes were filtered as described in Section 3.1, and binned into 20 logarithmically spaced mass bins spanning the range $\log_{10}(M_0/[h^{-1}M_\odot]) = 11.18$ to 14.42. Median mass profiles and CMHs of haloes, normalised by M_0, were used to calculate the concentration, c, and formation time, z_{-2}, for each M_0 and z_0. These were then converted to their equivalent values in "density space": c expressed in terms of the characteristic density $\langle\rho_{-2}\rangle$ (following Eq (1)), and z_{-2} in terms of the critical density, $\rho_{\rm crit}(z_{-2})$; both are then normalised by $\rho_{\rm crit}(z_0)$.

As shown in Figs. 4 and 5, the $\langle\rho_{-2}\rangle - \rho_{\rm crit}(z_{-2})$ relation for F6 haloes is similar to that in GR for most densities, but displays a steepening at high formation redshifts where $\langle\rho_{-2}\rangle$ increases more rapidly than $\rho_{\rm crit}(z_{-2})$. This effect is most apparent at lower redshifts (Fig. 4) and for lower masses (Fig. 5). For instance, only $f(R)$ halo mass bins with $\log_{10}(M_{200}/[h^{-1}M_\odot]) \lesssim 11.9$ at $z_0 = 0.5$, and with $\log_{10}(M_{200}/[h^{-1}M_\odot]) \lesssim 12.2$ at $z_0 = 0$ have $\log_{10}(\rho_{-2}/\rho_{\rm crit}(z_0)) > 4.25$, as shown by Figs. 4 and 5. This is consistent with the results found by Shi et al. (2015) for the concentration-mass and formation time-mass relations: while the formation times show small systematic differences between GR and F6, the biggest discrepancy between the two is in the form of the concentration-mass relation at low halo masses.

The concentrations recovered in the F6 model are *higher* for lower mass haloes than in GR, as demonstrated by Fig. 2; this change is in the opposite sense to that seen on changing CDM for WDM. In both WDM and F6, however, low

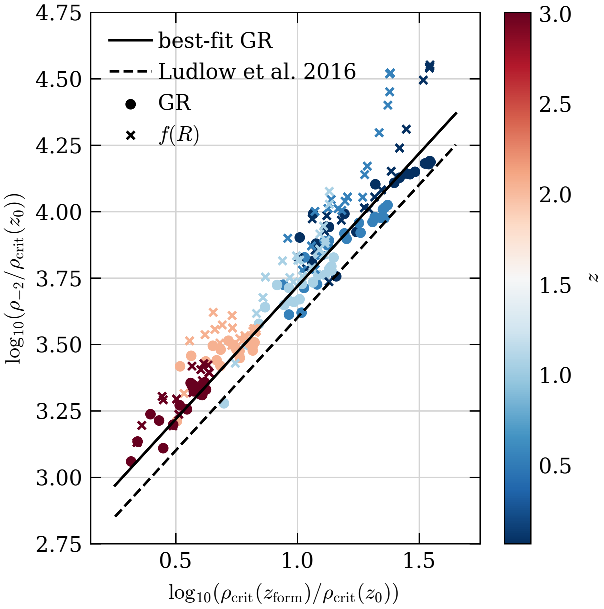

Figure 4. Mean enclosed density $\langle\rho_{-2}\rangle$ within the characteristic radius, r_{-2}, versus the critical density at the formation redshift, $\rho_{\rm crit}(z_{-2})$, at which a fraction $F = M_{-2}/M_0$ of the root halo mass M_0 was first contained in progenitors more massive than $f \times M_0$. Each point corresponds to median value in a logarithmically-spaced mass bin at the identification redshift z_0. All densities are normalised by $\rho_{\rm crit}(z_0)$, the critical density at z_0. Point types indicate the results from different gravities, as labelled. Colours indicate the identification redshift, as shown by the colour bar. Also plotted are two lines: a dashed black one which shows the Ludlow et al. (2016) scaling relation $\langle\rho_{-2}\rangle = 400 \times \rho_{\rm crit}(z_{-2})$, and a solid black one for the best-fitting GR relation $\langle\rho_{-2}\rangle = 525 \times \rho_{\rm crit}(z_{-2})$.

mass haloes systematically form later than their GR counterparts. In F6 gravity, although there is a systematic delay in formation histories for low-mass haloes, it is not captured by the formation time defined as in Eq (12).

It follows that, while in WDM the formation time-concentration relation is the same as it is in CDM (when $z_{\rm form}$ is appropriately defined), this is not the case in $f(R)$ gravity. Even a model with an effective screening mechanism, such as F6, affects the low mass haloes identified at late times; these objects have slightly delayed formation times and notably higher concentrations, which leads to the differences between F6 and GR shown in Figs. 4 and 5.

Finally, we note that the $\langle\rho_{-2}\rangle - \rho_{\rm crit}(z_{-2})$ relation found in the GR simulation is very similar to the one reported by Ludlow et al. (2016), but with a higher intercept, ≈ 525, as shown by the solid line in Fig. 4. The origin of this value, which is the only free parameter of their model, is not known. It is analogous to the free parameter of the Ludlow et al. (2014a) and Correa et al. (2015) models, who also report different values. The intercept may be determined by a number of physical process and a detailed investigation of what determines its value, while worthwhile, is beyond the scope of our paper.

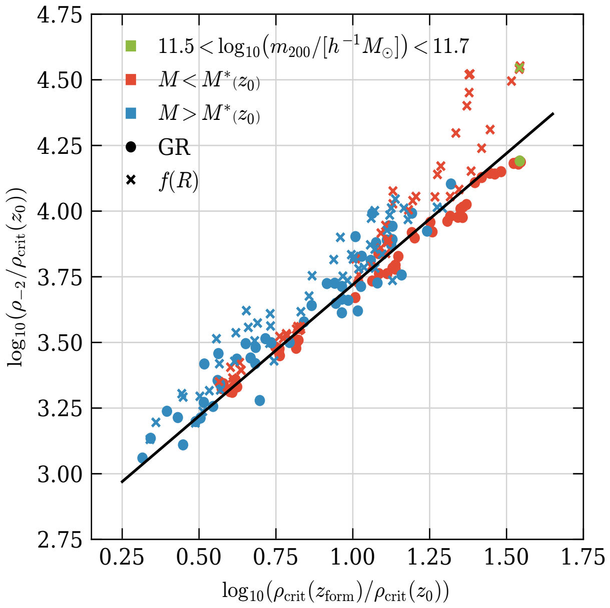

Figure 5. Same as Fig. 4, but colour–coded to indicate different halo mass ranges. The halo population has been split into two samples: one above and ones below the characteristic mass, $M^*(z_0)$, defined as $\delta_{\rm sc}(z_0)/\sigma(M^*(z_0)) = 1$ (Mo et al. 2010, Eq. 7.48). The mass bin containing haloes from Figs. 2 and 3 at z_0 is highlighted in green.

3.5 Sensitivity to variation of model parameters

The parameters used to construct the CMHs (and hence to estimate z_{-2}) and to define halo characteristic densities can be varied to assess their impact the form of the $\langle\rho_{-2}\rangle - \rho_{\rm crit}(z_{-2})$ relation, and to potentially improve our understanding of the origin of the difference between F6 and GR. A few such variations have been performed: first, we modify the radius defining halo characteristic densities (using $0.3 \times r_{-2}$ and $2.0 \times r_{-2}$), and second, the mass threshold f of progenitors included in the CMH (which is varied from 0.01 to 0.1).

The results, presented in Figs. 6 and 7, confirm our intuition: increasing the progenitor mass used to construct the CMHs (by increasing f) brings the formation time closer to the identification time, z_0 (the difference is more pronounced at lower redshifts, due to the normalisation used), while increasing the radius within characteristic densities are defined decreases the mean enclosed density *and* brings the formation time closer to the identification redshift. While the parameters can be tweaked to decrease the scatter and remove the time dependence of the relation (see, e.g., Figures B1 and B2 of Ludlow et al. 2016) the $f(R)$ haloes still exhibit a strong upwards trend in their concentrations–as well as a larger scatter than their GR counterparts–for all parameter combinations. This is driven by the changes to both the $c(M, z)$ relation, and also to changes in the mass–formation time relations, which cannot be accounted for by varying the parameters mentioned above. In $f(R)$ gravity, however, the halo growth and structure are also determined by the local environment. It is therefore important to attempt to account for local effects using an environmental proxy.

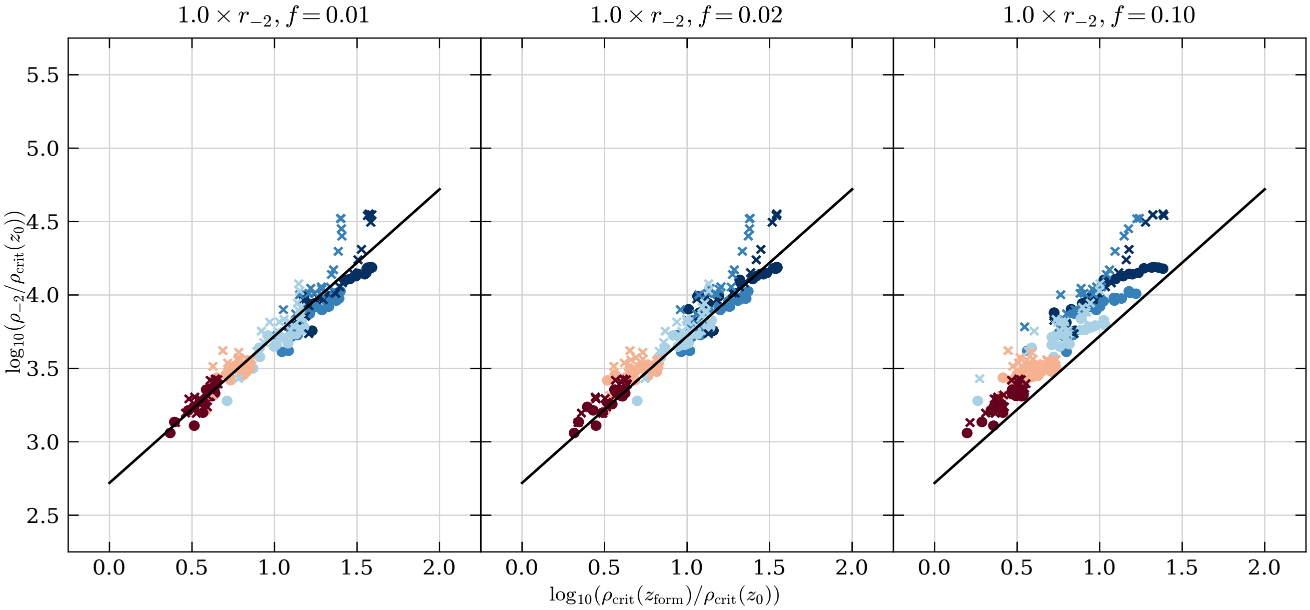

Figure 6. Like Fig. 4, but with different panels showing different collapsed mass history parameter f, as labelled above each. The solid black line shows the best-fitting GR relation, $\langle \rho_{-2} \rangle = 525 \times \rho_{\rm crit}$, and is included for comparison.

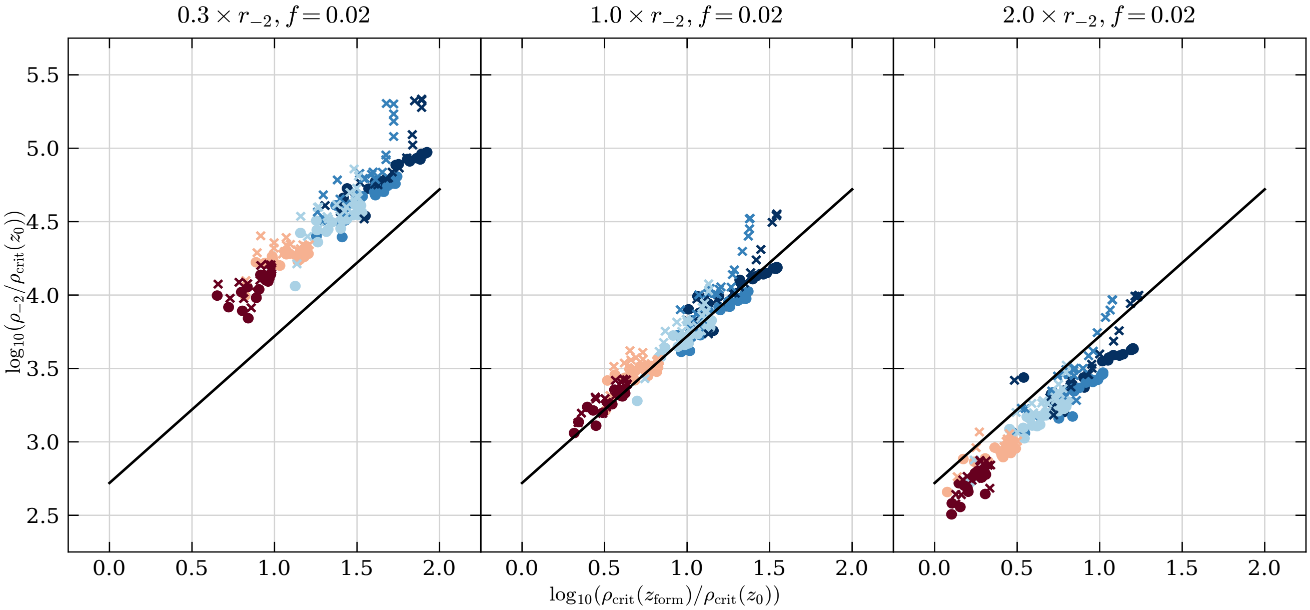

Figure 7. Like Fig. 4, but with different panels showing mean density at different fractions of a characteristic radius r_{-2}. The solid black line shows, for comparison, the best-fitting GR relation, $\langle \rho_{-2} \rangle = 525 \times \rho_{\rm crit}$.

3.6 Separation of haloes by screening

As discussed in Section 2.1, $f(R)$ gravity only affects haloes which are outside screened regions, while the screened ones grow in a manner that is largely indistinguishable from GR. It is clear from Fig. 4 that low mass haloes are typically the ones displaying the most prominent differences between the two simulations, implicating the fifth force as the root cause. However, it is natural that each mass bin contains both screened and unscreened objects.

The effectiveness of the screening mechanism (not including self-screening) is directly related to the environment in which the halo is found. Following Zhao et al. (2011); Haas et al. (2012), we use a conditional nearest neighbour distance, $D_{N,f}$, as an environmental proxy. We use the proxy in an attempt to separate haloes inside each mass bin into

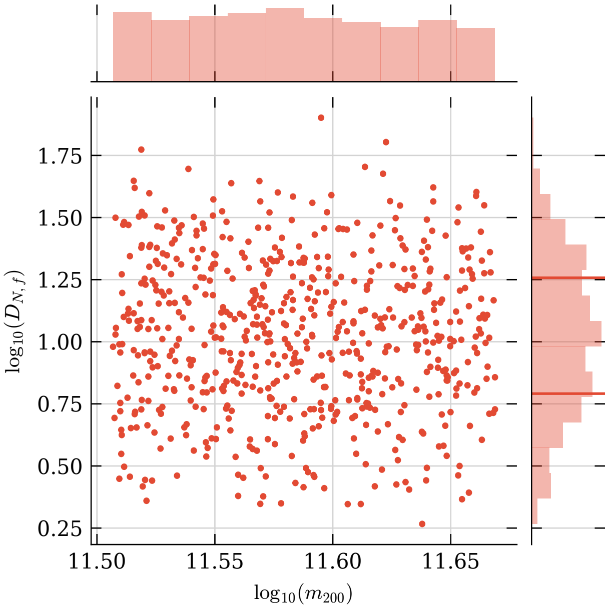

Figure 8. Environmental proxy $D_{N,f}$ ($N = 1$, $f = 1$) versus halo mass, M_{200}, for haloes in an example mass bin, $11.70 < \log_{10}\left(M_{200}/[h^{-1}M_{\odot}]\right) < 11.83$, at redshift $z = 0$. Distributions of $\log_{10}\left(M_{200}/[h^{-1}M_{\odot}]\right)$ and $\log_{10}\left(D_{N,f}\right)$ are shown at the top- and right-hand panels, respectively. The two red lines on the $\log_{10}\left(D_{N,f}\right)$ histogram on the right indicate the 25th and 75th percentiles.

two populations, quantifying how strong the environmental screening effect should be.

$D_{N,f}$ for a halo of mass $\bar{M}_{200}$ is defined as the distance d (normalised to $\bar{r}_{200}$) to its N^{th} nearest neighbouring whose mass, M_{200}, is equal to or larger than $f \times \bar{M}_{200}$. If $D_{N,f}$ cannot be calculated (for instance, for the largest halo in a snapshot) it is assumed to be equal to ∞.

Other environment proxies, such as “experienced gravity” Φ_* (Li et al. 2011) and local spherical or shell overdensity (Shi et al. 2017) have also been proposed as methods of assessing environmental impact on formation histories. Here we use $D_{N,f}$ with $N = 1$, $f = 1.0$ since it correlates strongly with other proxies, which predict similar local enhancements to the gravitational potential (Shi et al. 2017).

The $D_{N,f}$ values have been calculated for each halo at each redshift. Here we consider the distribution of $D_{N,f}$ in bins of halo mass focusing on the extremes of the distribution which we expect will show the biggest contrast in the efficiency of screening. The halo population at each redshift is split into two sub-groups: those below the 25th and above the 75th percentiles. The most massive object, with $D_{1,1} = \infty$, is excluded. The $\langle\rho_{-2}\rangle - \rho_{\text{crit}}(z_{-2})$ relations were then recalculated for each mass bin for the two sub-groups separately, and are presented in Fig. 9.

It is to be expected that the haloes with the lowest values of $D_{N,f}$, which are the ones that are closest to objects of comparable masses and hence in the highest density environments, will follow a concentration-formation relation closest to that displayed by GR haloes, since they are screened from the enhanced gravity. Haloes with high-$D_{N,f}$ may display a different power-law, as seen in Fig. 4. However, as clearly demonstrated in Fig. 9, while selecting haloes by their $D_{N,f}$ value has little to no effect on the GR relation, it also has little impact on the F6 haloes. This means that the difference cannot be easily accounted for by a local environmental proxy alone.

4 CONCLUSIONS

We have compared two high resolution dark matter only simulations, one using GR and the other F6 gravity. We constructed collapsed mass histories of haloes using their merger trees obtained from `HBT+` (Han et al. 2018). We then binned the haloes by mass and calculated median enclosed mass profiles $M(r)$ and CMHs, to obtain median concentrations, c, and formation times, z_{-2}, which we used to construct the $\langle\rho_{-2}\rangle - \rho_{\text{crit}}(z_{-2})$ relation. This relation is linear in GR–and hence may be used to predict concentrations when CMHs are known–but not in F6. The differences are primarily due to a relative *enhancement* of concentration for low-mass objects in F6 which have slightly *delayed* formation times times relative to GR.

We have made several attempts to recover a linear relation from the results of the F6 simulation. For example, we varied the free parameters of the model (i.e. the fraction f of the final halo mass that a progenitor must exceed to be included in the CMH, and fraction of the characteristic radius r_{-2} used to define the characteristic densities) to find a region in the parameter space which produces the most promising relation. While there are values of parameters which improve upon the conventional choice for GR ($f = 0.02$, $1.0 \times r_s$), there are trade-offs with regards to scatter and gradient of the line. Furthermore, to account for the mixing of the screened and unscreened haloes in each mass bin, we split the halo catalogue into two sub-populations using an environmental proxy $D_{N,f}$, which also had little effect.

Since neither approach alone has been successful, we propose that either (1) information about haloes' sizes *as well as* environment is required, or (2) a better proxy, capable of separating haloes not only by present environment, but also by their growth histories, is required, or (3) the density-density relation in $f(R)$ is not separable into the power law and a correction.

Our overall conclusion is that the form of the concentration–formation time relation is particular to the gravitational force in the adopted cosmological model and its origin remains unknown. The key difficulty seems to lie in the question of why haloes with very similar formation redshifts can nevertheless have very different concentrations. One possibility is that the definition of formation time (z_{-2}) or assembly history (CMH)–which function well for GR models for $c(M, z)$–require amendments for $f(R)$.

Since the relation is sensitive to model parameter variation, but not to environment–based splitting, it would be interesting to further test the relation for a dependence on self-screening. This could be tested by splitting halo populations using a self-screening proxy, as well as running the analysis on other cosmologies, such as F5, F4 and enhanced (4/3 the conventional strength) gravity simulations. We believe that looking into the changes in the concentration –

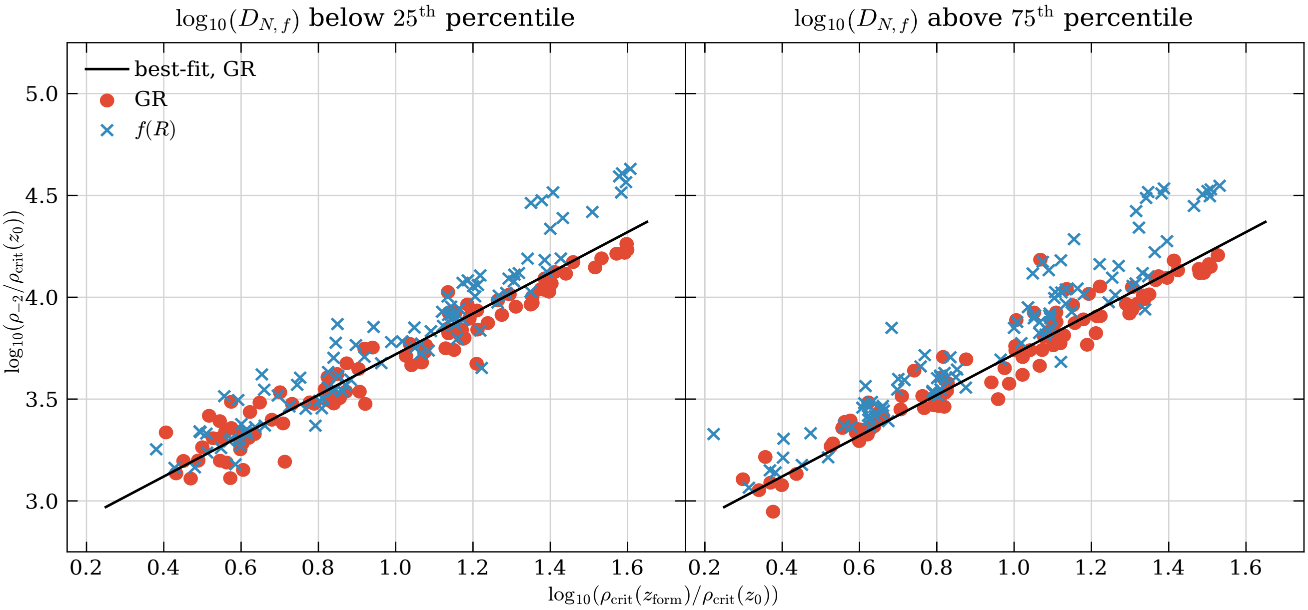

Figure 9. Like Fig. 4, but split into two populations by the environmental proxy $D_{N,f}$. The left panel shows the relation for bins including haloes below the 25th percentile; the right panel shows the same relation for bins including haloes above the 75th percentile. Colours and symbols distinguish between gravity models: red circles represent GR and blue crosses F6. Both panels include the best fitting GR relation $\langle\rho_{-2}\rangle = 525 \times \rho_{\rm crit}$ (solid black line) for reference (note that the fit is performed over the full population, regardless of the environmental proxy).

formation relation in different gravity regimes is a promising avenue of research into the nature and origin of the correlation between halo concentrations and formation times.

ACKNOWLEDGEMENTS

We thank Difu Shi for helpful discussions and for providing simulation outputs. This work was supported by the Science and Technology facilities Council ST/P000541/1. PO acknowledges an STFC studentship funded by STFC grant ST/N50404X/1. ADL acknowledges financial supported from the Australian Research Council through their Future Fellowship scheme (project number FT160100250).This work used the DiRAC@Durham facility managed by the Institute for Computational Cosmology on behalf of the STFC DiRAC HPC Facility (www.dirac.ac.uk). The equipment was funded by BEIS capital funding via STFC capital grants ST/K00042X/1, ST/P002293/1, ST/R002371/1 and ST/S002502/1, Durham University and STFC operations grant ST/R000832/1. DiRAC is part of the National e-Infrastructure.

REFERENCES

Akaike H., 1974, IEEE Transactions on Automatic Control, 19, 716

Angel P. W., Poole G. B., Ludlow A. D., Duffy A. R., Geil P. M., Mutch S. J., Mesinger A., Wyithe J. S. B., 2016,] 10.1093/mnras/stw737, 459, 2106

Berry C. P. L., Gair J. R., 2011, Physical Review D, 83

Bond J. R., Cole S., Efstathiou G., Kaiser N., 1991, The Astrophysical Journal, 379, 440

Bose S., Hellwing W. A., Li B., 2015, Journal of Cosmology and Astroparticle Physics, 2015, 034

Bose S., Hellwing W. A., Frenk C. S., Jenkins A., Lovell M. R., Helly J. C., Li B., 2016, Monthly Notices of the Royal Astronomical Society, 455, 318

Buchdahl H. A., 1970, Monthly Notices of the Royal Astronomical Society, 150, 1

Bullock J. S., Kolatt T. S., Sigad Y., Somerville R. S., Kravtsov A. V., Klypin A. A., Primack J. R., Dekel A., 2001, Monthly Notices of the Royal Astronomical Society, 321, 559

Carroll S. M., Duvvuri V., Trodden M., Turner M. S., 2004, Physical Review D, 70

Cataneo M., et al., 2015, Physical Review D, 92, 044009

Clifton T., Ferreira P. G., Padilla A., Skordis C., 2012, Physics Reports, 513, 1

Correa C. A., Wyithe J. S. B., Schaye J., Duffy A. R., 2015, Monthly Notices of the Royal Astronomical Society, 452, 1217

Davis M., Efstathiou G., Frenk C. S., White S. D. M., 1985, The Astrophysical Journal, 292, 371

Diemer B., Joyce M., 2019, The Astrophysical Journal, 871, 168

Diemer B., Kravtsov A. V., 2015, The Astrophysical Journal, 799, 108

Duffy A. R., Schaye J., Kay S. T., Dalla Vecchia C., 2008,] 10.1111/j.1745-3933.2008.00537.x, 390, L64

Einasto J., 1965. Trudy Astrophys. Inst., Alma-Ata

Gao L., Navarro J. F., Cole S., Frenk C. S., White S. D. M., Springel V., Jenkins A., Neto A. F., 2008, Monthly Notices of the Royal Astronomical Society, 387, 536

Gunn J. E., Gott III J. R., 1972, The Astrophysical Journal, 176, 1

Haas M. R., Schaye J., Jeeson-Daniel A., 2012, Monthly Notices of the Royal Astronomical Society, 419, 2133

Han J., Jing Y. P., Wang H., Wang W., 2012, Monthly Notices of the Royal Astronomical Society, 427, 2437

Han J., Cole S., Frenk C. S., Benitez-Llambay A., Helly J., 2018, Monthly Notices of the Royal Astronomical Society, 474, 604

He J.-h., Guzzo L., Li B., Baugh C. M., 2018, Nature Astronomy

Hernández-Aguayo C., Baugh C. M., Li B., 2018, Monthly Notices of the Royal Astronomical Society, 479, 4824

Hinshaw G., et al., 2013, The Astrophysical Journal Supplement Series, 208, 19

Hu W., Sawicki I., 2007, Physical Review D, 76

Jiang L., Helly J. C., Cole S., Frenk C. S., 2013, ResearchGate

Joyce A., Jain B., Khoury J., Trodden M., 2015, Physics Reports, 568, 1

Khoury J., Weltman A., 2004, Physical Review Letters, 93, 171104

Klypin A., Yepes G., Gottlöber S., Prada F., Heß S., 2016, Monthly Notices of the Royal Astronomical Society, 457, 4340

Koyama K., 2016, Reports on Progress in Physics, 79, 046902

Lacey C., Cole S., 1993, Monthly Notices of the Royal Astronomical Society, 262, 627

Li B., Mota D. F., Barrow J. D., 2011, The Astrophysical Journal, 728, 109

Li B., Zhao G.-B., Teyssier R., Koyama K., 2012, Journal of Cosmology and Astroparticle Physics, 2012, 051

Lombriser L., 2014, Annalen der Physik, 526, 259

Lombriser L., Koyama K., Li B., 2014, Journal of Cosmology and Astroparticle Physics, 2014, 021

Ludlow A. D., Navarro J. F., Springel V., Vogelsberger M., Wang J., White S. D. M., Jenkins A., Frenk C. S., 2010, Monthly Notices of the Royal Astronomical Society, 406, 137

Ludlow A. D., et al., 2013, Monthly Notices of the Royal Astronomical Society, 432, 1103

Ludlow A. D., Navarro J. F., Angulo R. E., Boylan-Kolchin M., Springel V., Frenk C., White S. D. M., 2014a, Monthly Notices of the Royal Astronomical Society, 441, 378

Ludlow A. D., Borzyszkowski M., Porciani C., 2014b,] 10.1093/mnras/stu2021, 445, 4110

Ludlow A. D., Bose S., Angulo R. E., Wang L., Hellwing W. A., Navarro J. F., Cole S., Frenk C. S., 2016, Monthly Notices of the Royal Astronomical Society, 460, 1214

Ludlow A. D., Schaye J., Bower R., 2018, arXiv e-prints

Maccio A. V., Dutton A. A., Van Den Bosch F. C., Moore B., Potter D., Stadel J., 2007, Monthly Notices of the Royal Astronomical Society, 378, 55

Macciò A. V., Dutton A. A., van den Bosch F. C., 2008, Monthly Notices of the Royal Astronomical Society, 391, 1940

Macciò A. V., Ruchayskiy O., Boyarsky A., Muñoz-Cuartas J. C., 2013,] 10.1093/mnras/sts078, 428, 882

Mo H., van den Bosch F., White S., 2010, Galaxy Formation and Evolution. Cambridge University Press, `http://www.astro.yale.edu/vdbosch/book.html`

Moore B., Governato F., Quinn T., Stadel J., Lake G., 1998, The Astrophysical Journal Letters, 499, L5

Navarro J. F., Frenk C. S., White S. D. M., 1996, The Astrophysical Journal, 462, 563

Navarro J. F., Frenk C. S., White S. D. M., 1997, The Astrophysical Journal, 490, 493

Neto A. F., et al., 2007, Monthly Notices of the Royal Astronomical Society, 381, 1450

Nunes R. C., Pan S., Saridakis E. N., Abreu E. M. C., 2017, Journal of Cosmology and Astroparticle Physics, 2017, 005

Peebles P. J. E., 1980, The Large-Scale Structure of the Universe. Princeton Series in Physics, Princeton University Press, Princeton, N.J

Planck Collaboration et al., 2016, Astronomy & Astrophysics, 594, A1

Power C., Navarro J. F., Jenkins A., Frenk C. S., White S. D. M., Springel V., Stadel J., Quinn T., 2003, Monthly Notices of the Royal Astronomical Society, 338, 14

Prada F., Klypin A. A., Cuesta A. J., Betancort-Rijo J. E., Primack J., 2012,] 10.1111/j.1365-2966.2012.21007.x, 423, 3018

Schmidt F., Lima M., Oyaizu H., Hu W., 2009, Physical Review D, 79

Schwarz G., 1978, The Annals of Statistics, 6, 461

Shi D., Li B., Han J., Gao L., Hellwing W. A., 2015, Monthly Notices of the Royal Astronomical Society, 452, 3179

Shi D., Li B., Han J., 2017, Monthly Notices of the Royal Astronomical Society, 469, 705

Terukina A., Lombriser L., Yamamoto K., Bacon D., Koyama K., Nichol R. C., 2014, Journal of Cosmology and Astroparticle Physics, 2014, 013

Thomas P. A., Muanwong O., Pearce F. R., Couchman H. M. P., Edge A. C., Jenkins A., Onuora L., 2001, Monthly Notices of the Royal Astronomical Society, 324, 450

Thomas P. A., et al., 2015, arXiv:1508.05388 [astro-ph]

Upadhye A., Steffen J. H., 2013, arXiv:1306.6113 [astro-ph]

Wechsler R. H., Bullock J. S., Primack J. R., Kravtsov A. V., Dekel A., 2002, The Astrophysical Journal, 568, 52

Zhao D. H., Jing Y. P., Mo H. J., Brner G., 2003, The Astrophysical Journal, 597, L9

Zhao D. H., Jing Y. P., Mo H. J., Börner G., 2009, The Astrophysical Journal, 707, 354

Zhao G.-B., Li B., Koyama K., 2011, Physical Review Letters, 107

Zuntz J., Zlosnik T. G., Bourliot F., Ferreira P. G., Starkman G. D., 2010, Physical Review D, 81

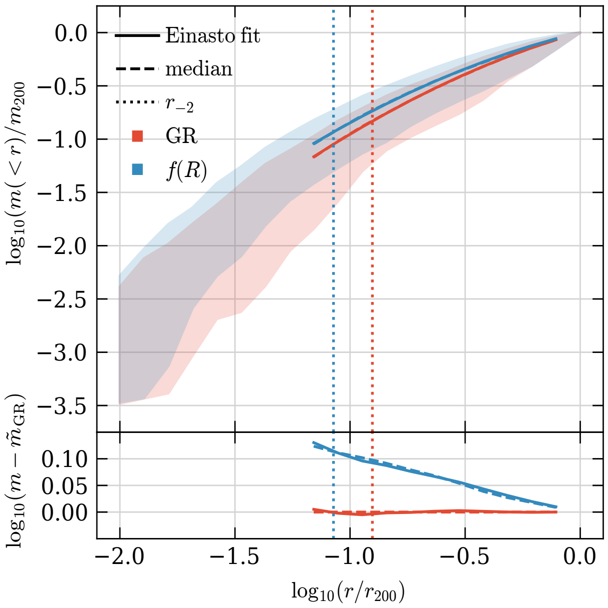

Figure A1. Like Fig. 2, but fit to the Einasto density profile.

APPENDIX A: EINASTO PROFILE

The Einasto density profile (Einasto 1965) can be expressed as

$$\ln\left(\frac{\rho}{\rho_{-2}}\right) = -\frac{2}{\alpha}\left[\left(\frac{r}{r_{-2}}\right)^{\alpha} - 1\right], \tag{A1}$$

where r_{-2} is a scale radius (at which where the logarithmic slope of the density profile is equal to -2), and α is a "shape" parameter.

Fits using both NFW and Einasto density profiles have been performed for comparison. We have computed and compared model selection criteria, called AIC and BIC, as an objective way to determine if the additional parameter in the Einasto profile is justified in terms of improved fits to the simulation results (Akaike 1974; Schwarz 1978). The AIC and BIC measures take into account the χ^2 value of the fit and the number of free parameters. The fit with the smallest value of AIC or BIC is deemed to be the most appropriate one to use[5].

The Einasto density profiles for an illustrative mass bin at $z_0 = 0$ are shown in Fig. A1; the CMHs for the same mass bin at $z_0 = 0$, for values of F calculated from Einasto concentrations, are shown in Fig. A2. Table A1 shows values the values of the AIC and BIC statistics for the NFW fits from Section 3.2 and the Einasto fits from this section. Despite the fact that the Einasto profile produces a better fit, it has an extra free parameter, which yields higher values of the information criteria. This indicates that the NFW profile is the more justified choice.

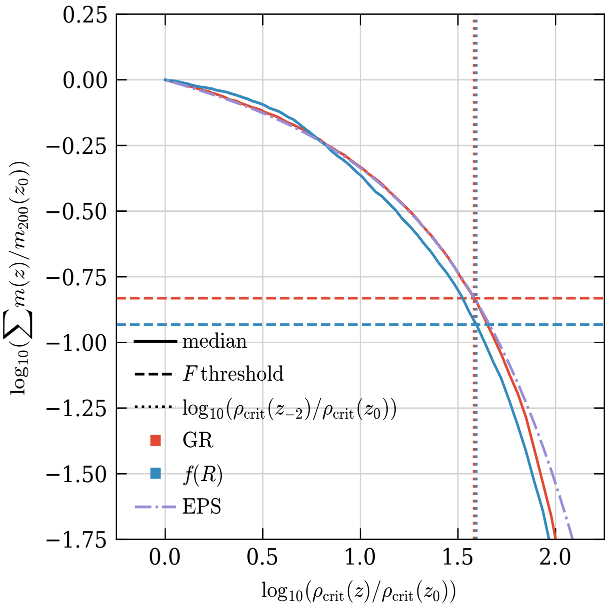

Figure A2. Like Fig. 3, but for the values of F calculated from Einasto concentrations from Fig. A1.

Table A1. Goodness-of-fit comparison between the NFW and Einasto density profiles for haloes with masses in the range $11.5 < \log_{10}\left(M_{200}/[h^{-1}M_\odot]\right) < 11.7$ at $z_0 = 0$ for the GR run.

	NFW	Einasto
number of parameters	1	2
AIC	2.002	2.399
BIC	4.002	4.797

---

[5] There is a subtle difference between the AIC and BIC statistics. BIC introduces a higher penalty for more complicated models; however, this is only important if the criteria give conflicting results, which is not the case here